

# Fluid dynamic mechanisms of enhanced power generation by closely spaced vertical axis wind turbines

Stefania Zanforlin<sup>1,\*</sup> and Takafumi Nishino<sup>2</sup>

<sup>1</sup> Department of Energy, Systems, Territory and Constructions Engineering, University of Pisa, I.go Lucio Lazzarino, 56122 Pisa, Italy.

<sup>2</sup> Centre for Offshore Renewable Energy Engineering, Cranfield University, Cranfield, Bedfordshire MK43 0AL, UK.

\* Corresponding author. Tel.: +39-050-2217145; fax: +39-050-2217150; e-mail address: s.zanforlin@ing.unipi.it.

## Abstract

We present a comprehensive set of two-dimensional (2D) unsteady Reynolds-averaged Navier-Stokes (URANS) simulations of flow around a pair of counter-rotating vertical-axis wind turbines (VAWTs). The simulations are performed for two possible configurations of the counter-rotating VAWT pair, with various gaps between the two turbines, tip-speed-ratios and wind directions, in order to identify key flow mechanisms contributing to the enhanced performance of a pair of turbines compared to an isolated turbine. One of the key mechanisms identified, for the case of two turbines arrayed side-by-side with respect to the incoming wind, is the change of lateral velocity in the upwind path of each turbine due to the presence of the neighbouring turbine, making the direction of local flow approaching the turbine blade more favourable to generate lift and torque. The results also show that the total power of a staggered pair of turbines cannot surpass that of a side-by-side pair of turbines. Some implications of the present results for the prediction of the performance of single and multiple rows (or a farm) of VAWTs are also discussed. The local flow mechanisms identified in the present study are expected to be of great importance when the size of the farm is relatively small.

**Key words:** Counter-rotating VAWTs; Wind farm; Induced velocity; Blockage effect; Wake effect.

## Introduction

Following the rapid development of onshore and offshore wind farms in recent years, there is increasing interest in *how to improve the overall performance of multiple wind turbines*. Whilst a number of studies on horizontal-axis wind turbines (HAWT's) have shown the importance of spacing between the turbines (as well as the array configuration) to minimise the wake loss, recent studies on a closely spaced array of vertical-axis wind turbines (VAWT's) by Dabiri and his team [1-3] have shown the possibility of achieving a much higher power density (i.e., power per unit farm area) compared to existing wind farms

40 employing HAWT's. During their field measurements in Southern California in 2010 and 2011, Dabiri and  
41 his team [2, 3] tested various configurations of pairs of counter-rotating VAWT's closely spaced from each  
42 other, inspired by the hydrodynamic mechanism of "fish schooling" minimising the wake loss. The  
43 performance of pairs of counter-rotating VAWT's has also been investigated numerically by Feng et al. [4]  
44 using a free vortex method with empirical wake models. More recently, Araya et al. [5] has proposed a low-  
45 order model of two-dimensional flow past pairs of VAWT's using the concept of a leaky Rankine body,  
46 showing the existence of two competing fluid dynamic mechanisms (namely the local acceleration of the  
47 flow and local deceleration of the flow) that contribute to the overall array performance.

48 The exact mechanisms of the enhanced power generation by closely spaced pairs of VAWT's,  
49 however, are still unclear since these previous studies have not revealed detailed local flow characteristics  
50 around each turbine sufficiently. Hence in this study, we perform a comprehensive set of two-dimensional  
51 unsteady Reynolds-averaged Navier-Stokes (URANS) simulations of a single and a pair of counter-rotating  
52 VAWT's, to compare detailed local flow characteristics around the turbine blades and thereby identify key  
53 fluid dynamic mechanisms that explain the increased performance of a pair of turbines relative to an isolated  
54 turbine. The simulations are performed for two possible configurations of the counter-rotating turbine pair,  
55 with various gaps between the two turbines, tip-speed-ratios and wind directions. The results show clearly  
56 how, and why, the values of torque generated during the upwind path and downwind path of each turbine are  
57 affected by the presence of the neighbouring turbine. Although this study is concerned with vertical-axis  
58 wind turbines, the majority of the findings and conclusions obtained in this study are applicable to vertical-  
59 axis tidal/marine turbines as well.

60 It should be noted that a number of Computational Fluid Dynamics (CFD) studies of a vertical-axis  
61 turbine using 2D URANS simulations have already been reported in the past. A recent extensive review of  
62 these CFD studies can be found in [6]. A general consensus from these earlier CFD studies is that carefully  
63 designed 2D URANS simulations are capable of predicting the influence of the turbine on the flow around  
64 the turbine as well as the performance of the turbine qualitatively correctly, especially for an H-shape  
65 Darrieus turbine with a high aspect ratio (which helps minimise 3D flow effects). Nevertheless, the majority  
66 of the earlier CFD studies have focused on the performance of a single turbine; investigations into the  
67 interaction of two vertical-axis turbines closely spaced from each other are still limited.

68 This study is based on the 1.2 kW Windspire VAWT [7], a commercial turbine for micro-generation.  
69 The diameter of the turbine ( $D$ ) is 1.20 m, the chord length ( $c$ ) is 0.128 m and therefore the solidity  
70 ( $\sigma = B \cdot c / (\pi \cdot D)$ , where  $B=3$  is the blade number) is 0.10, which is typical for medium-high solidity VAWTs  
71 for urban areas. We chose this turbine for three reasons. The first reason is the availability of experimental  
72 data taken by the manufacturer in an open field, which avoids the need to correct wind tunnel data by taking  
73 into account blockage effects. The second reason is its large aspect ratio (the ratio of blade length to turbine  
74 diameter is 5) that reduces the influence of 3D aerodynamics (associated with blade tip losses), allowing a  
75 comparison of 2D CFD results with the experimental data. The third reason is the possibility of a comparison  
76 with earlier studies in the literature, i.e. this turbine has been used in the aforementioned experimental and

77 numerical campaign carried out by Dabiri and his team [1-3] and, more recently, in the numerical analysis by  
78 Feng et al. [4].

79

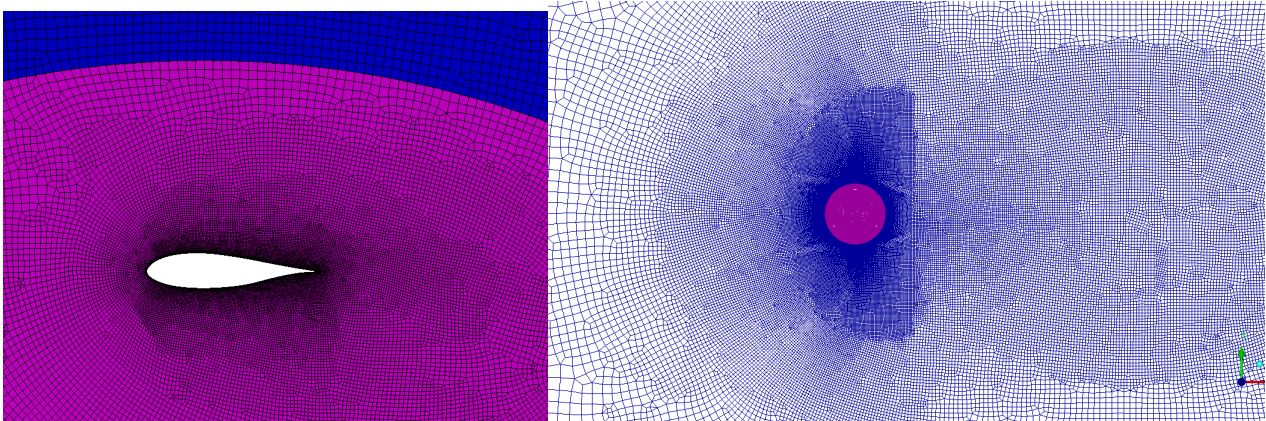
## 80 **Model set-up**

81

82 We start by constructing a computational domain using the commercial mesh generator ANSYS  
83 ICEM. The size of the computational domain is 57D (35D in upstream, 22D in downstream) along the x-  
84 coordinate, and 100D along the y-coordinate, where D is the turbine diameter. The positions of inlet and  
85 lateral boundaries are far enough for the flow to be considered unbounded, i.e., the boundaries have  
86 negligible influence on the characteristics of the flow oncoming the turbine. The position of the outlet  
87 boundary allows a complete wake development.

88 Two different grid levels are adopted: a fixed sub-grid with the external dimensions of the flow  
89 domain, and one (or two, in case of a turbine pair) rotating sub-grid that includes the VAWT geometry and  
90 allows a relative motion with respect to the fixed grid. This grid arrangement utilises the sliding mesh  
91 technique [8] and allows the simulation of the rotational motion of the turbine with an unsteady Reynolds-  
92 averaged Navier-Stokes (URANS) analysis. The grids are everywhere unstructured with the exception of the  
93 region around the blades, where 14 structured layers of quad elements are set to better predict the boundary  
94 layer phenomena. The grids are finer near the blade surface (and in particular where flow separation occurs  
95 due to dynamic stall) and progressively coarser outward. As shown in figure 1 a high density grid is also set  
96 in the near wake region and far downstream to accurately simulate the wake development and any  
97 aerodynamic interferences between the wakes of a turbine pair.

98



99

100 FIGURE 1: (left) details of the grid around the blades and (right) in the near/far wake regions (only a part of the whole domain is  
101 shown); different colours indicate the rotating and the fixed sub-grids.

102

103 The number of grid points around the airfoil profile (suction plus pressure sides) is 440. The wall distance  
104 from the first layer of cells is set at  $2.3 \cdot 10^{-4}c$ , where  $c$  is the blade chord length, resulting in the maximum  $y^+$   
105 (dimensionless wall distance) of less than 3 (except for the trailing edge region, where  $y^+ < 5$ ). The rotating  
106 sub-grid consists of  $\sim 120,000$  elements (for each one, in case of a turbine pair); the fixed sub-grid consists of  
107  $\sim 130,000$  and  $\sim 150,000$  elements for a single turbine and a pair of turbines, respectively. Across the inlet, the  
108 Dirichlet boundary condition is specified with a uniform velocity  $U_0$  of  $8.0 \text{ ms}^{-1}$ . According to typical built

109 environments, the turbulence intensity and length scale are set to 4% and 1m, respectively, at the inlet. The  
 110 upper and lower boundary conditions are set to a symmetric condition. At the exit boundary, a fixed pressure  
 111 equal to the free stream condition is specified.

112 Computations were performed using the commercial CFD solver ANSYS FLUENT v.15, using its  
 113 “pressure-based” segregated solver for the URANS equations. Turbulence is modelled using the k- $\omega$  SST  
 114 (Shear Stress Transport) model. The principle behind the SST model is the combination of two different  
 115 turbulence models: the k- $\omega$  model in the inner part of the boundary layer, and the k- $\epsilon$  model in the free-  
 116 stream. This turbulence scheme was adopted because of its aptitude in cases involving high adverse pressure  
 117 gradients and therefore smooth surface separations [9]; it has proved to be particularly efficient for VAWTs  
 118 due to its ability to simulate more accurately the vortices that are seen during dynamic stall at low TSR than  
 119 the k- $\omega$  and k- $\epsilon$  models [10]. The air is considered as incompressible since the operating conditions do not  
 120 exceed a local Mach number greater than 0.3. The settings for the simulations are shown in table 1. The  
 121 convergence criteria is set at  $1 \cdot 10^{-4}$  for all residuals. Thirty turbine revolutions are simulated: for the first 20  
 122 rev. a coarse time-step corresponding to  $2^\circ$  azimuthal angle of turbine rotation is used; for the successive 10  
 123 rev. a finer time-step corresponding to  $0.5^\circ$  azimuthal angle is used.

124

<b>Solver</b>	
Type	Pressure-based
Time	Transient
<b>Solution methods</b>	
Pressure-Velocity coupling	PISO
<b>Spatial discretization</b>	
Gradient	Least squares cell based
Pressure	PRESTO!
Momentum	Second order upwind
Turbulent kinetic energy	Second order upwind
Specific dissipation rate	Second order upwind
<b>Transient formulation</b>	
Second order implicit	

TABLE 1: Settings for the CFD simulations

125

126

## 127 **Model validation**

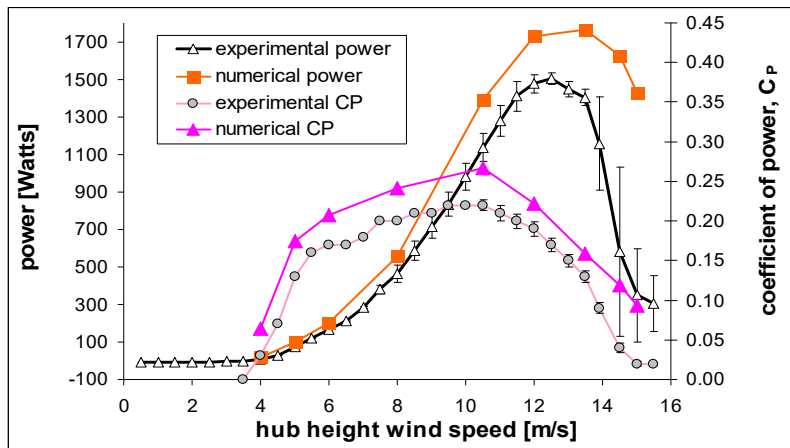
128

129 The blade profile of the 1.2 kW Windspire VAWT is an asymmetric airfoil DU06W200, designed at  
 130 the Delft University of Technology by adding 2% of thickness and a cambering of 0.8% to the symmetric  
 131 NACA0018 profile. Experimental force coefficients can be found in the thesis work of Claessens [11]. The  
 132 turbine operates with variable angular velocity,  $\Omega$ , by means of an electronic control system that allows to  
 133 maintain the tip speed ratio ( $TSR=R \cdot \Omega / U_0$ , where  $R=0.6m$  is the turbine radius) at an optimal value of 2.3  
 134 and the power coefficient ( $C_p=P/(0.5 \cdot \rho \cdot U_0^3 \cdot D)$ , where  $P$  is the power per meter of blade, and  $\rho$  is the air  
 135 density) at approximately 0.22. The load is controlled by passive stall: for wind speed lower than 10.6 m/s  
 136 (the rated wind speed) the TSR is kept to 2.3, but for higher wind speeds the turbine speed is kept constant

137 and thus the TSR decreases leading to stall. The relatively high solidity and the small size of the turbine  
 138 justify the low values of both  $C_p$  and the optimal TSR. In fact the operational average Reynolds number  
 139 ( $Re=c*R*\Omega/\nu$ , where  $\nu$  is the kinematic viscosity) is very low ( $\sim 160,000$  for  $U_0=8$  m/s), entailing  
 140 considerable flow separation phenomena induced by the high adverse pressure gradient occurring on the  
 141 blade suction side (as already discussed in a previous study, [12]).

142 We performed CFD simulations of an isolated turbine first to verify the numerical model by comparing  
 143 results with experimental data. Figure 2 shows a comparison between the calculated and the experimental  
 144 values of power and  $C_p$  versus the wind speed measured at the hub height. Except for very low wind speeds  
 145 (that imply extremely low Reynolds numbers) and very high wind speeds (that involve stall), the numerical  
 146 results compare well with the measured data; the differences are less than 20%, which is reasonable  
 147 considering that the experimental power is the electrical one and the CFD model includes neither the  
 148 interferences of shaft and struts nor the blade tip losses. Some additional simulations were made to verify the  
 149 grid sensitivity, as reported in the Appendix.

150



151

152 FIGURE 2: (left) Windspire 1.2kW VAWT; (right) comparison between experimental performance [7] and predictions obtained for  
 153 the Windspire turbine with ANSYS Fluent CFD software.

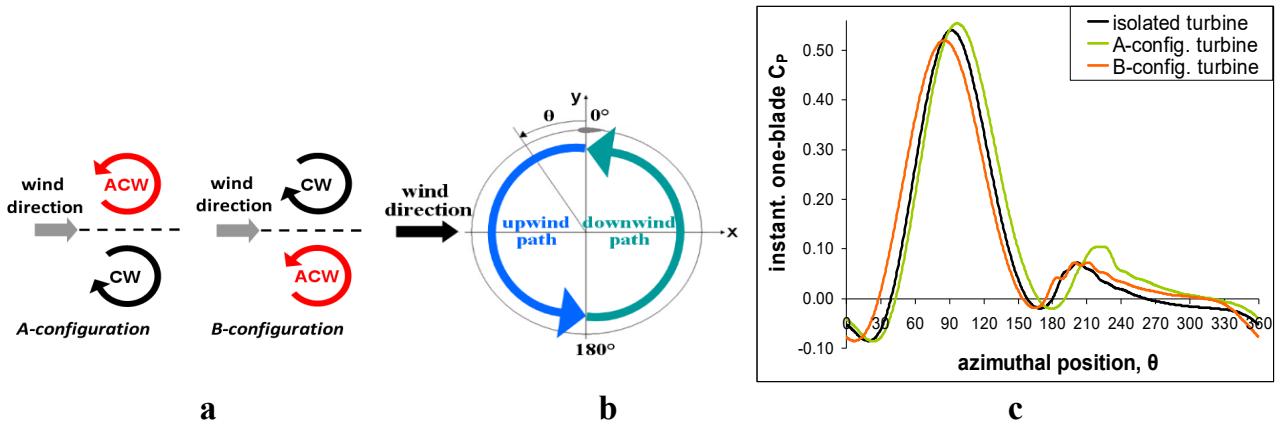
154

### 155 Physical mechanisms of a pair of turbines

156

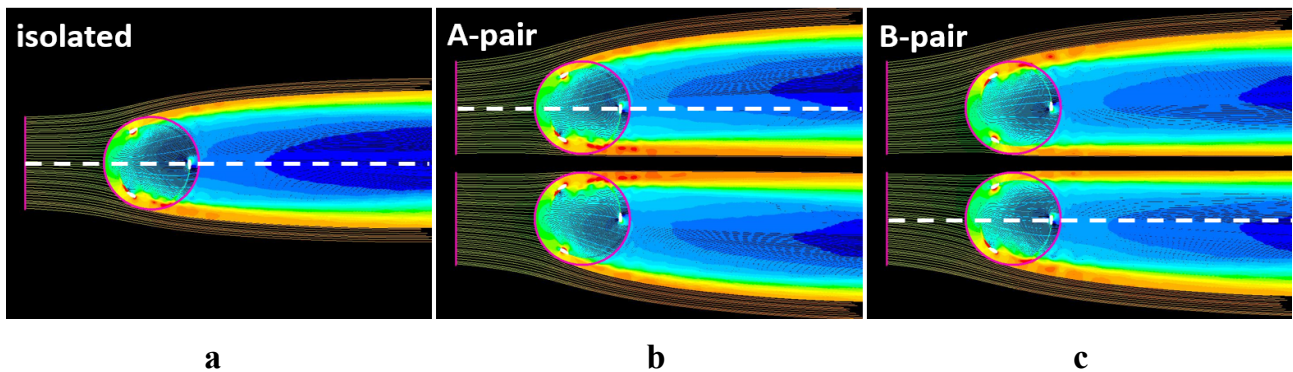
157 We analyse the behaviour of a pair of counter-rotating VAWTs in close proximity by means of 2D  
 158 CFD simulations. Two possible configurations “A” and “B” (see the schematic on figure 3 for the layout  
 159 definitions) are considered. All the simulations are performed for a wind speed of 8.0 m/s. Unless otherwise  
 160 specified, the distance between the two turbine axes is set at 1.5D and TSR is set at 2.7, which is the TSR  
 161 giving the highest power for the turbine pair cases.

162 A schematic representation of the upwind and downwind paths of the blade in one revolution is given  
 163 in figure 3; as usually done, in all graphs illustrating the instantaneous  $C_p$  for a single blade, the azimuthal  
 164 position  $\theta=0$  corresponds to the beginning of the upwind path of the blade. It should be observed that a blade  
 165 starts its upwind path from the outer side of the configuration in case of A, and from the inner side of the  
 166 configuration in case of B. In all comparative analyses of this study the isolated turbine is considered to spin  
 167 anticlockwise.



171 FIGURE 3: (a) Definition for the layout of configurations A and B; (b) schematic representation of the upwind and downwind paths  
 172 of the blade in one revolution; (c) one-blade  $C_p$  during one revolution calculated for the isolated (anticlockwise) turbine and for the  
 173 anticlockwise turbine in configurations A and B.  
 174

175 Before quantitatively analysing the performance of counter-rotating VAWT pairs, we highlight some  
 176 qualitative features that can be found comparing the streamlines around a pair of VAWTs to those around an  
 177 isolated turbine (figure 4).  
 178



181 FIGURE 4: Streamlines coloured with velocity magnitude [ $1 \pm 10.5$  m/s] for the isolated turbine (a), A-pair (b) and B-pair (c); to  
 182 facilitate the comparison, only the streamlines starting from grid cells intercepted by the magenta lines (the same for all the pictures)  
 183 are shown; white dashed lines indicate the anticlockwise turbines.  
 184

185 (a) Due to rotation, an isolated turbine shows a slight *wake bending*; hence the wakes of A-  
 186 configuration turbines diverge in the lateral ( $y$ ) direction slightly more than the wakes of B-  
 187 configuration turbines.

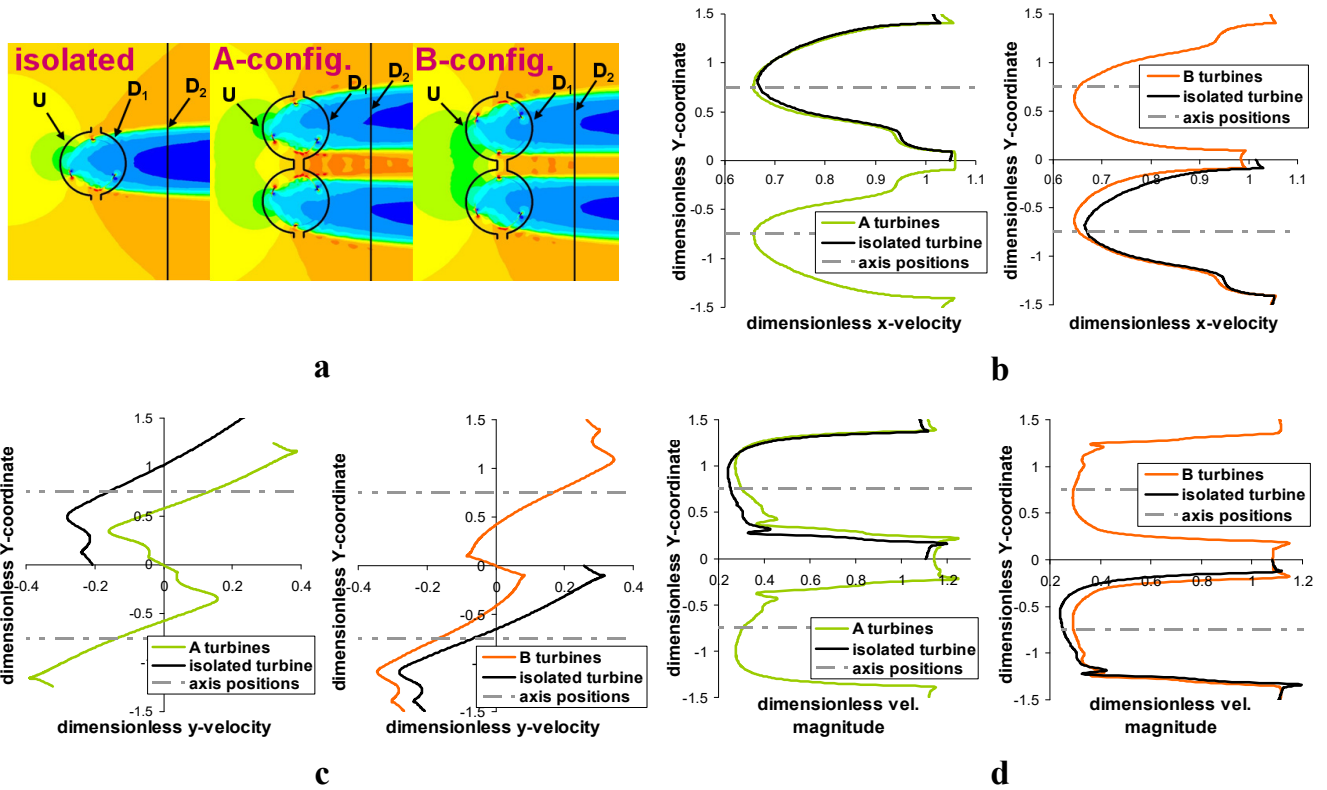
188 (b) Due to streamwise resistance imposed by the turbine(s), flow tends to accelerate outside of each  
 189 turbine (as with an ideal actuator disc). In case of A, however, flow accelerates more significantly  
 190 through the gap between the two turbines, whereas in case of B, the flow acceleration between the two  
 191 turbines is less pronounced. The difference between A and B lies in the direction of the velocity  
 192 induced by the rotors (which is concordant with the wind direction for A and discordant for B). As a  
 193 result, more flow tends to go outside of the two turbines for B than for A.



194 (c) The streamlines approaching the turbines at the inner sides of the pair configuration are constrained  
 195 parallel to the configuration symmetry plane, whereas for an isolated turbine the flow is induced to  
 196 diverge at both sides.

197 (d) A significant *wake contraction* is observed at the inner sides of pair configuration (the width of the  
 198 inner half of a wake appears noticeably reduced). The outer half of the wake does not change  
 199 appreciably.

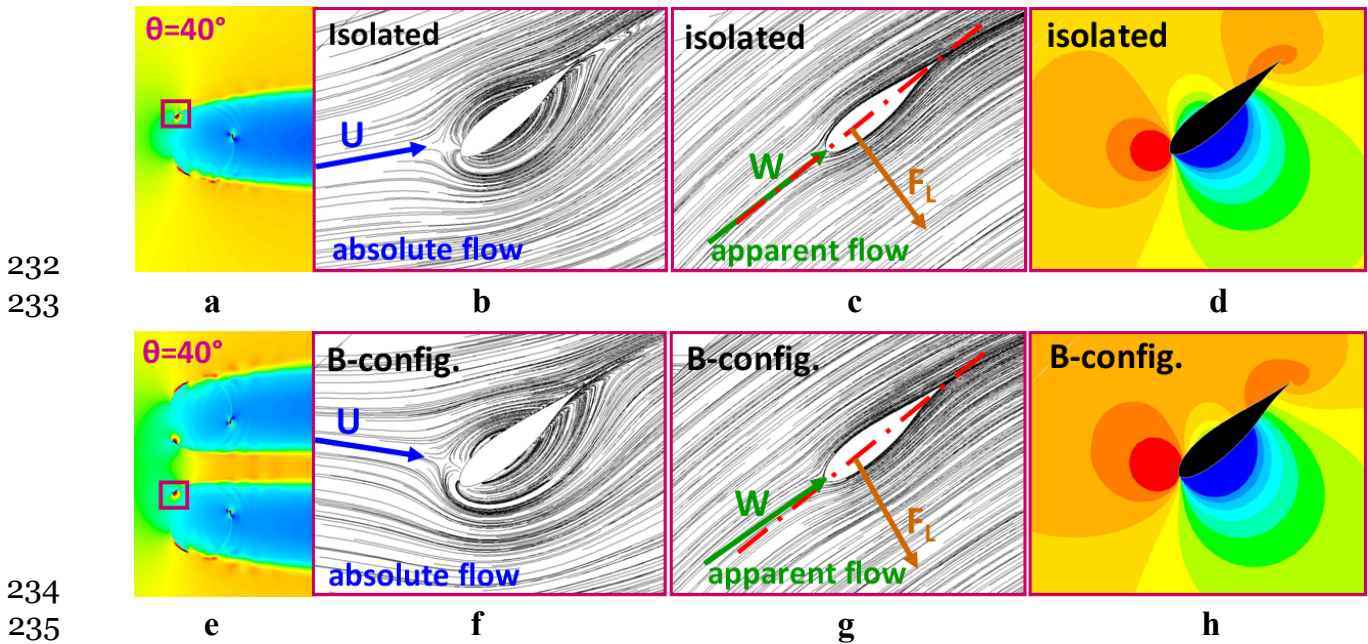
200 We examined x and y-components of the flow velocity upstream the turbines (on U-curve), near-  
 201 downstream (on  $D_1$ -curve) and far-downstream (on  $D_2$ -line). The results are plotted in figure 5 (results  
 202 concerning  $D_2$ -line are omitted for brevity) together with velocity magnitude maps and curve setting. The  
 203 velocity values for the isolated turbine are shifted along y-coordinate to facilitate the comparison with the  
 204 turbine belonging to the A and B configurations and spinning in the same rotational direction. Also, the  
 205 velocities and distances have been non-dimensionalised by the velocity at the inlet,  $U_0$ , and the rotor  
 206 diameter,  $D$ , respectively. It should be noted that: (1) the decrease of x-velocities on U-curve suggests a  
 207 reduction of the flow rate through the turbines, especially for the B-pair; (2) y-velocities are greatly reduced  
 208 during the early upwind path for B and during the late upwind path for A (namely, at the inner sides of the  
 209 configuration); and (3) as a consequence of the reduced flow rate through the turbines, a moderate increase  
 210 of y-velocities occurs during the early upwind path for A and during the late upwind path for B (namely, at  
 211 the outer sides of the configuration).



212 FIGURE 5: (a) Velocity magnitude maps [ $1 \div 10.5 \text{m/s}$ ] for the isolated turbine and for the side-by-side A and B configurations, and  
 213 the curves set to compare the velocity components; (b) dimensionless x-velocity on U-curve; (c) dimensionless y-velocity on U-  
 214 curve; (d) dimensionless velocity magnitude on  $D_1$ -curve. Results refer to a particular time step of the unsteady solution (blades at  $0^\circ$ ,  
 215  $120^\circ$  and  $240^\circ$  azimuthal degrees).  
 216

217 The velocity plots in figure 5 can explain the power increase in the upwind path and in the downwind  
 218 path achieved with both configurations A and B with respect to the isolated turbine, shown by the one-blade  
 219 instantaneous  $C_p$  graph in figure 3. The gain in the upwind path comes from an extension of the azimuthal  
 220 range in which torque is generated; in particular the torque generation ends later for A and begins earlier for  
 221 B. Importantly, this range extension is correlated to the suppression of y-velocity component (or the  
 222 component diverging from the turbine axis) in the flow approaching the blade at the inner sides of  
 223 configuration, as will be illustrated below.

224 To justify how the suppression of y-velocity in the flow approaching the blades during the upwind path  
 225 can increase torque generation, we compare local flow characteristics around a blade for an isolated turbine  
 226 and a turbine in B-configuration at an azimuthal position  $\theta=40^\circ$  (beginning of the upwind path). Figure 6  
 227 depicts absolute and relative (or apparent) streamlines. It can be seen that the aerodynamic interaction  
 228 between the two turbines of the B-configuration modifies the direction of the absolute flow approaching the  
 229 blade and therefore the direction of the apparent flow (namely, the flow observed from the rotating blade).  
 230 As a consequence, for the turbine belonging to the B-pair there is a component of lift in tangential direction  
 231 (responsible for torque generation), whereas for the isolated turbine there is not.



232  
 233  
 234  
 235  
 236 FIGURE 6: Isolated turbine vs. B-configuration: (a, e) velocity magnitude maps [ $1\div 11\text{m/s}$ ]; (b, f) absolute and (c, g) apparent  
 237 streamlines for the flow around the blade at  $\theta=40^\circ$  (blue and green arrows indicate the direction of absolute and apparent flows,  
 238 respectively; brown arrows indicate the direction of the lift force); (d, h) absolute pressure maps [ $-250\div 170\text{ Pa}$ ].

240 The absolute pressure maps for B-configuration show a greater pressure difference between the pressure and  
 241 the suction sides of the blade and therefore a higher lift, confirming the better performance achievable with a  
 242 pair of counter-rotating turbines in B-configuration at  $40^\circ$  azimuth. It should be noted that this result is  
 243 obtained despite a lower flow rate (lower x-velocities) for B-configuration, demonstrating the importance of  
 244 the direction of the flow approaching the blade. Qualitatively similar results were observed comparing a  
 245 turbine in A-configuration with an isolated turbine during the late upwind path (not shown here for brevity).



246 The power gain observed in the downwind path by both configurations with respect to the isolated  
 247 turbine (see  $C_p$  graph in figure 3) is more difficult to interpret, but it appears to be largely due to higher flow  
 248 rates occurring in the near-downstream (as proved by velocity magnitude monitored on  $D_1$ -curve) as a  
 249 consequence of the wake contraction. This happens because at the inner sides of the configuration the flow  
 250 through the downwind path is prevented to diverge laterally (as it would happen at both sides of an isolated  
 251 turbine) by the presence of the second turbine, and thus it is constrained parallel to the configuration  
 252 symmetry plane, accompanied by a contraction of the wake width.

253 We can conclude that if the turbines are aligned side-by-side, two physical mechanisms are responsible  
 254 for the enhanced performance of counter-rotating VAWT pairs: (1) *y-velocity suppression in the upwind path*  
 255 that makes the direction of the flow approaching the blade more favourable to generate lift and torque, and  
 256 (2) *wake contraction in the downwind path*.

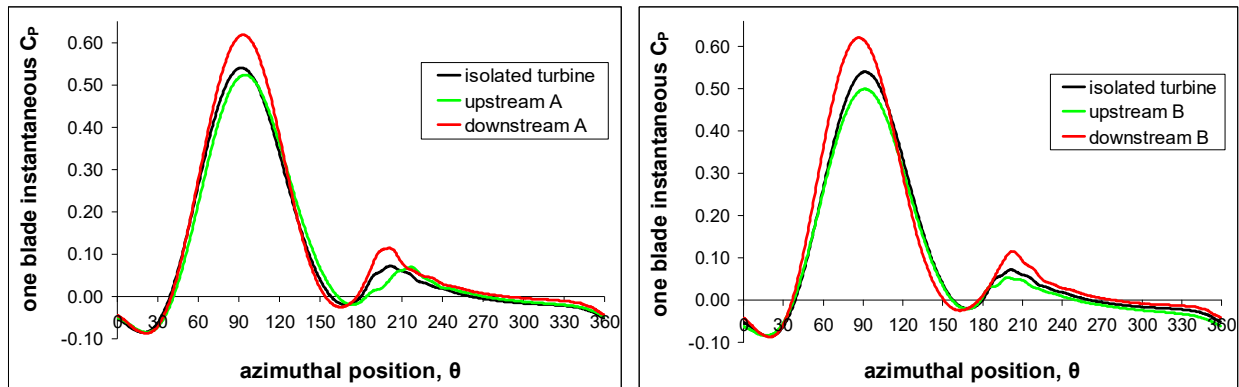
257

### 258 Effect of staggering the two turbines

259

260 Do these mechanisms also occur in case of staggered pairs? We investigated the behaviour of  
 261 staggered A and B pairs with distances between turbine axes  $\Delta x=1.5D$  and  $\Delta y=1.5D$ . Results are depicted in  
 262 figures 7 and 8. The instantaneous one-blade  $C_p$  graphs in figure 7 show a significant performance  
 263 improvement for the downstream turbine for both A and B pairs and also a (less significant) performance  
 264 deterioration for the upstream turbine for the B pair.

265



266

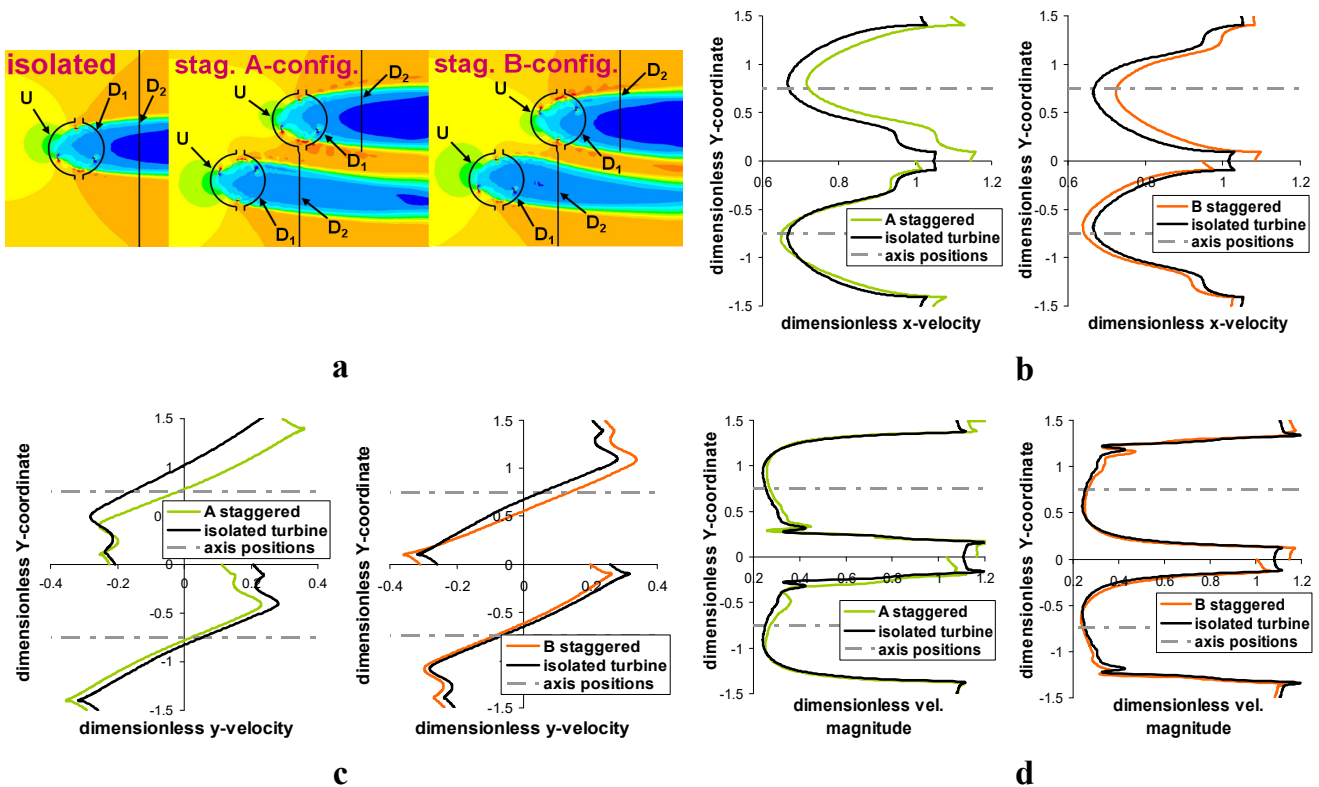
267 FIGURE 7: Instantaneous one-blade  $C_p$  for the upstream and the downstream A turbines (left) and for the upstream and the  
 268 downstream B turbines (right), compared to the isolated turbine.

269

270 The mechanism responsible for the good performance of the downstream turbine, however, is rather different  
 271 from that found for side-by-side pairs. Here the dominant mechanism is an *effect of the upstream turbine*  
 272 *blockage*. In particular, the high flow rate occurring at the sides of the upstream turbine contributes to the  
 273 peak  $C_p$  of the downstream turbine that is considerably higher than that of the isolated turbine (without the  
 274 extension of the azimuthal range producing torque observed for the side-by-side configurations). Moreover,  
 275 most of the power gain, with respect to the isolated turbine, is generated in the upwind path. Reasons for  
 276 these results can be found by looking at the plots of the flow velocity monitored on U and  $D_1$  curves in figure  
 277 8; the values for the isolated turbine are shifted along y-coordinate and also mirrored (duplicated) to facilitate

278 the comparison with the turbines spinning in the same rotational direction. X-velocities on U-curve confirm  
 279 the much higher flow rate in front of the downstream turbines, whereas y-velocities are quite similar to that  
 280 calculated for the isolated turbine. Velocity magnitudes on  $D_1$  curve exhibit only a slight increase and  
 281 indicate the absence of any wake contraction for the downstream turbine. These results suggest that both y-  
 282 velocity suppression and wake contraction beneficial mechanisms occur only when the turbines are aligned  
 283 side-by-side.

284 Meanwhile, the poorer performance found for the upstream B-turbine can be explained by considering  
 285 the convergent wake bending, i.e. a shorter distance between the two turbine wakes for the B-pair compared  
 286 to that for the A-pair. Due to the presence of the downstream turbine preventing a complete wake  
 287 development, the flow rate through the upstream turbine is reduced, as shown by the reduction of the x-  
 288 velocity values on U-curve in figure 8. It should be noted that for the staggered B-pair the x-velocity  
 289 reduction is observed across the entire width of the upstream turbine, whereas for the side-by-side B-pair the  
 290 x-velocity reduction is observed only on the inner side of the upstream turbine, as shown earlier in figure 5.  
 291 As will be shown later, the convergent wake bending of B-pairs will also be responsible for an earlier  
 292 performance drop for the downstream turbine when the y-distance between the turbine axes is gradually  
 293 shortened, since the downstream turbine will be in the wake of the upstream turbine more likely for the B-  
 294 pair than for the A-pair.

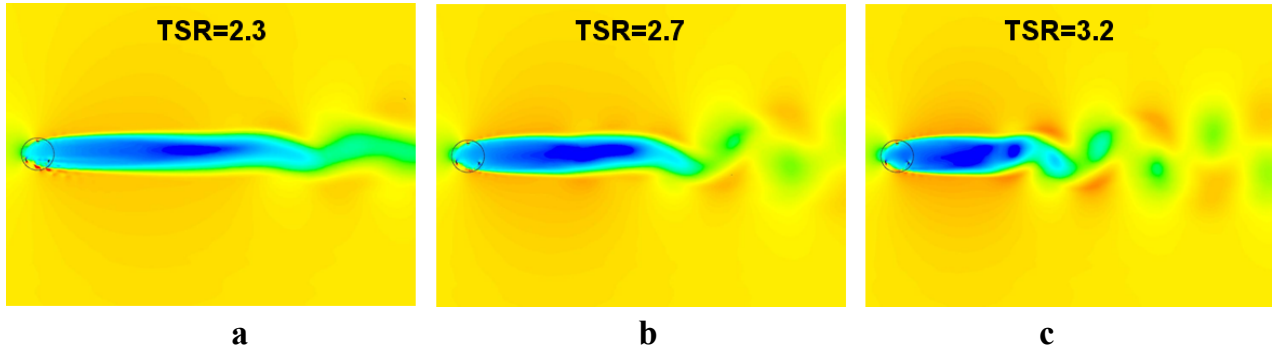


295 FIGURE 8: (a) Velocity magnitude maps [ $1 \div 10.5 \text{ m/s}$ ] for the isolated turbine and for the staggered A and B configurations, and the  
 296 curves set to compare the velocity components; (b) Dimensionless x-velocity on U-curve; (c) Dimensionless y-velocity on U-curve;  
 297 (d) Dimensionless velocity magnitude on  $D_1$ -curve. Results refer to a particular time step of the unsteady solution (blades at  $0^\circ$ ,  $120^\circ$   
 298 and  $240^\circ$  azimuthal degrees).  
 299  
 300

301 **Effect of TSR**

302  
303  
304  
305  
306  
307

Before discussing the effects of TSR on a turbine pair, the effects on an isolated turbine are briefly illustrated. As can be seen on the velocity magnitude maps in figure 9, an increase in TSR leads to a reduction of the turbine permeability, making the turbine more and more similar to a bluff body (as revealed by the wake shortening and the growth of wake instabilities far downstream).

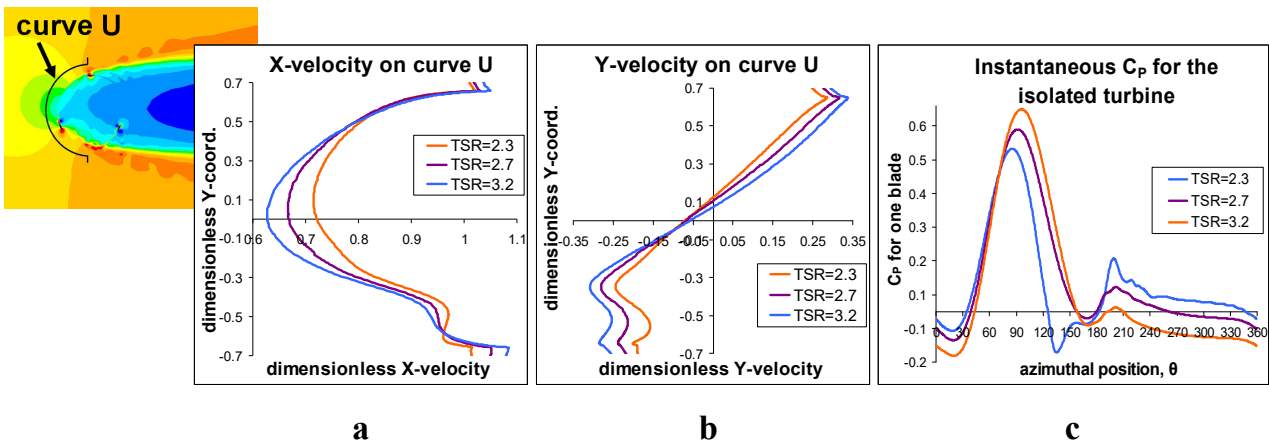


308  
309  
310

FIGURE 9: Velocity magnitude maps [ $1 \div 10.5 \text{m/s}$ ] for the isolated turbine at TSR=2.3 (a), 2.7 (b), 3.2 (c).

311  
312  
313  
314  
315  
316  
317  
318

The permeability reduction mainly involves two effects observed in the plots of the velocity components upstream the turbine (on U-curve) reported in figure 10: a reduction of the flow rate through the turbine (see the x-velocity decreasing) and an increasing of the flow rate at the turbine sides (see the increase of x- and, especially, of y-velocities). As noticeable in the graph of the instantaneous  $C_p$  in figure 10, the former is responsible for a torque decrement throughout the downwind path of the blade, whereas the latter is responsible for a delay in torque production during the upwind path.



319  
320  
321  
322  
323  
324

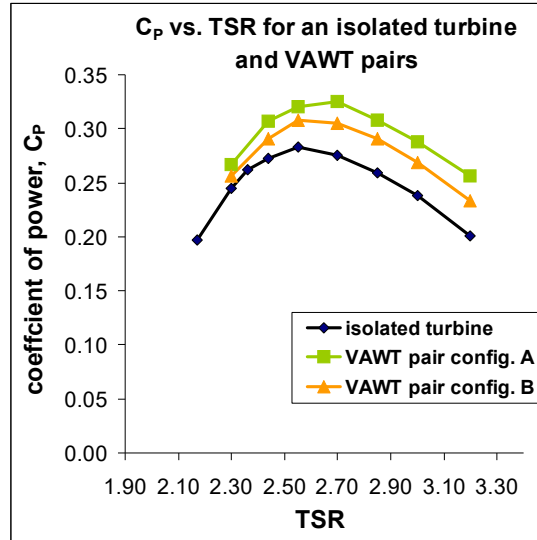
FIGURE 10: Dimensionless x-velocity (a) and dimensionless y-velocity (b) calculated on U-curve for the isolated turbine at TSR=2.3, 2.7, 3.2; (c) one-blade instantaneous  $C_p$  during one revolution, calculated for the isolated turbine at TSR=2.3, 2.7, 3.2. Results in (a) and (b) refer to a particular time step of the unsteady solution (blades at  $0^\circ$ ,  $120^\circ$  and  $240^\circ$  azimuthal degrees).

325  
326  
327  
328  
329

It should also be noted that, as already mentioned earlier, the turbine studied here is characterised by a relatively worse performance because of low operational  $Re$  that, especially at low TSR (as  $TSR=2.3$ ), generates flow separation and dynamic stall. Yet, flow separation is moderate at  $TSR=2.7$  and it completely disappears at  $TSR=3.2$ ; this explains the growth of the  $C_p$  peak value and its occurrence at larger azimuthal angles as the TSR increases.

330 Now we look at the effects of TSR on a (non-staggered) pair of turbines. As can be seen from the  
 331 graph in figure 11, both configurations A and B yield a relative power gain (referring to the turbine spinning  
 332 at the same TSR) especially at higher TSR. It can also be seen that A-configuration gives a better  
 333 performance than B-configuration.

334



335

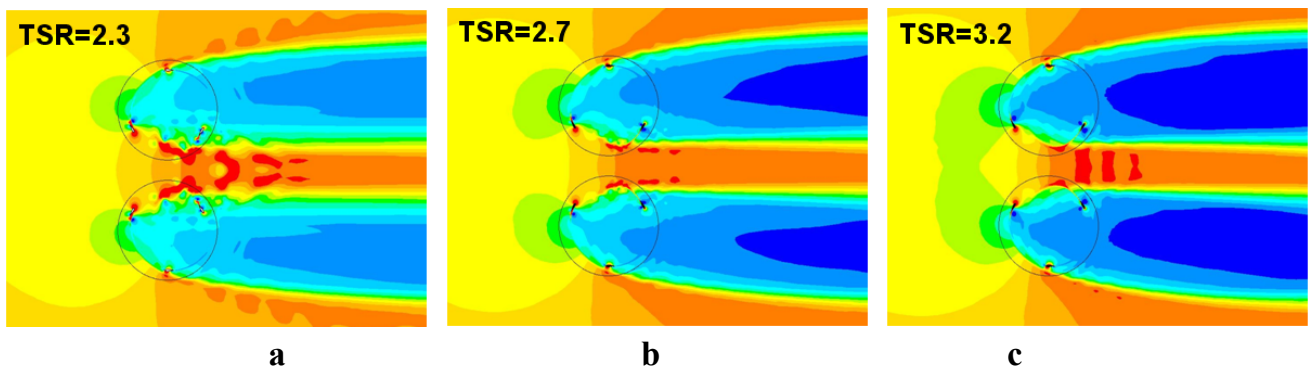
336

337

FIGURE 11:  $C_p$  versus TSR, calculated for the isolated turbine and for A and B-configurations.

338 The following analysis is focused on A-configuration since its better performance relative to B-  
 339 configuration makes possible a clearer description. To physically explain the increase of power gain obtained  
 340 (relatively to the isolated turbine) as the TSR increases, we first show that the permeability reduction found  
 341 for the isolated turbine is even emphasized in case of a pair of turbines. This can be seen from the velocity  
 342 magnitude maps in figure 12.

343



344

345

346

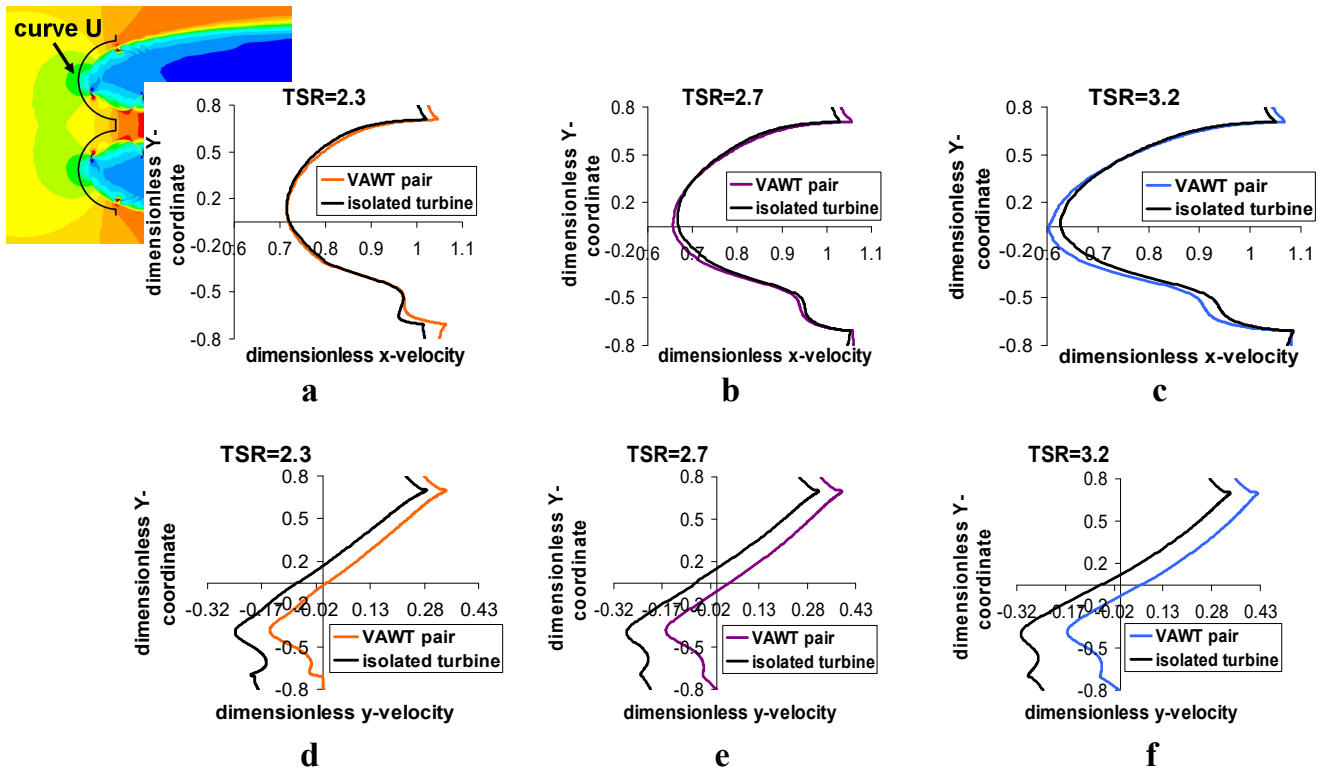
347

FIGURE 12: Velocity magnitude maps [ $1 \div 10.5 \text{m/s}$ ] for A-configuration, calculated at TSR=2.3 (a), 2.7 (b), 3.2 (c).

348 To further investigate the effects of TSR, x- and y-velocity components upstream of the turbines at  
 349 TSR=2.3, 2.7, 3.2 are presented in figure 13. Here we can see that an increase in TSR accentuates three main  
 350 effects on the interactions between the two turbines. Firstly, as the TSR increases the permeability decreases  
 351 with respect to the isolated turbine (as recognized by the decrease of x-velocity upstream of the turbines).  
 352 Secondly, following the permeability reduction, higher flow rates occur at the outer sides of the

353 configuration (as recognized by the x- and y-velocities increasing at the outer sides). Higher values of y-  
 354 velocity at the outer sides (with respect to the isolated turbine) delay the torque production at the beginning  
 355 of the upwind path (which means that the torque production starts later as the TSR increases). Thirdly, a  
 356 *drastic reduction of y-velocity upstream of the turbines at the inner sides of the configuration* occurs as the  
 357 TSR increases, resulting in a significant extension of torque production during the late part of the upwind  
 358 path. This last effect seems the main cause for the increase of the relative power gain with TSR, as will be  
 359 described below.

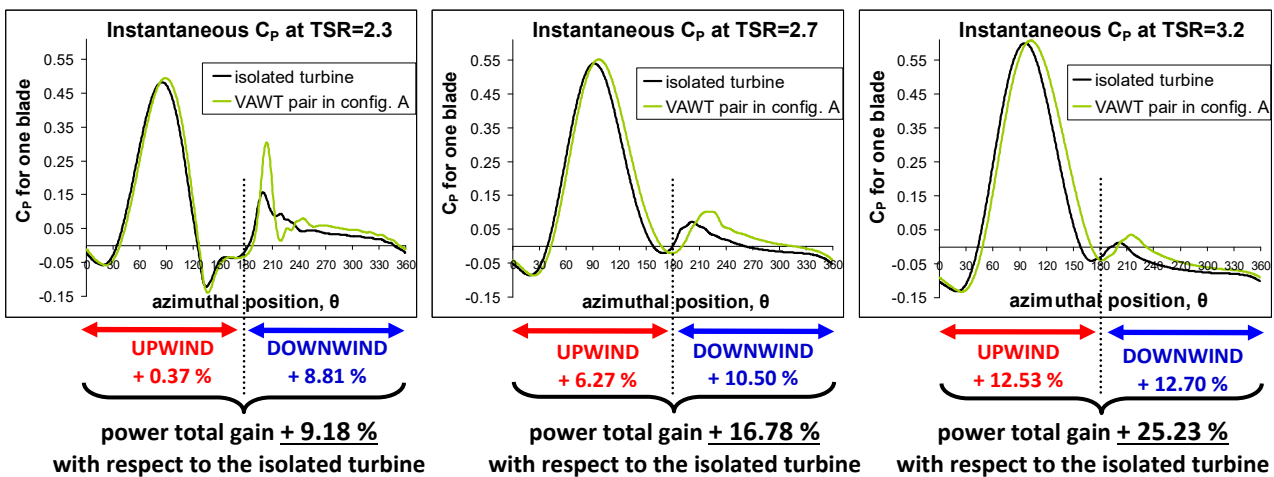
360  
 361



362 FIGURE 13: Dimensionless x-velocity (a, b, c) and dimensionless y-velocity (d, e, f) calculated at TSR=2.3, 2.7, 3.2 on U-curve for the isolated (anticlockwise spinning) turbine and for the upper (anticlockwise spinning) turbine of A-configuration. Results refer to a particular time step of the unsteady solution (blades at 0°, 120° and 240° azimuthal degrees).

366 In figure 14 a comparison of the one-blade instantaneous  $C_p$  curves for A configuration and for the isolated  
 367 turbine is presented for three TSR values, together with the percentages of power gains achieved during the  
 368 upwind and downwind paths.

369



370  
 371  
 372  
 373



374  
375  
376  
377  
378

**a**

**b**

**c**

FIGURE 14: One-blade instantaneous  $C_p$  during one revolution calculated for the isolated turbine and for A-configuration at TSR=2.3 (a), 2.7 (b), 3.2 (c); percentages of power gains with respect to the isolated turbine spinning at the same TSR are reported.

379 It is interesting to observe that the percentage of power gain obtained in the upwind path increases more and  
380 more as the TSR increases. However, as also well known from the actuator disk theory, the absolute  
381 maximum power is not obtained at the highest TSR since a too high TSR dramatically reduces the flow rate  
382 through the turbine, leading to excessively low wind speed in the downwind path (as already seen in the  
383 velocity maps in figure 12) and consequently to even negative torque in the downwind path (as noticeable in  
384 the one-blade instantaneous  $C_p$  graphs). Thus the best compromise between the upwind and downwind  
385 torque productions is achieved at TSR=2.7, as already shown in figure 11.

386 To conclude this section we remark that, although the physical mechanisms responsible for the power  
387 increasing in the upwind and downwind paths are expected to be valid for many different types of vertical  
388 axis (wind and tidal) turbines, the superiority of one configuration (A or B) and the benefit repartition  
389 between the upwind and downwind paths may depend on the turbine solidity and the fluid properties (or the  
390 Reynolds number).

391

#### 392 **Effects of wind direction and distance between turbines**

393

394 Wind direction ( $\gamma$ ) does not affect the power of an isolated VAWT, but does affect the power of a pair  
395 of VAWTs. The graph in figure 15 shows the effect of wind direction on the normalised power coefficient K  
396 (defined as the ratio of the turbine's  $C_p$  to the isolated turbine's  $C_p$ ) predicted for the anticlockwise (ACW)  
397 turbine. Note that this turbine pair can be seen as A-configuration or B-configuration, depending on the wind  
398 direction. The distance between the turbine axes is  $2D$  and TSR is 2.7 for both turbines, which corresponds  
399 to the optimal TSR found for a pair of turbines placed side-by-side, whereas the TSR for the reference  
400 isolated turbine is 2.55, which corresponds to the optimal TSR found for the isolated turbine. At  $\gamma=270^\circ$  the  
401 ACW turbine is located directly downstream of the clockwise (CW) turbine; for this wind direction the K  
402 value is not calculated, i.e. we assume the turbine is stopped ( $C_p=0$ ) since the absolute wind speed oncoming  
403 the turbine is below the cut-in limit.

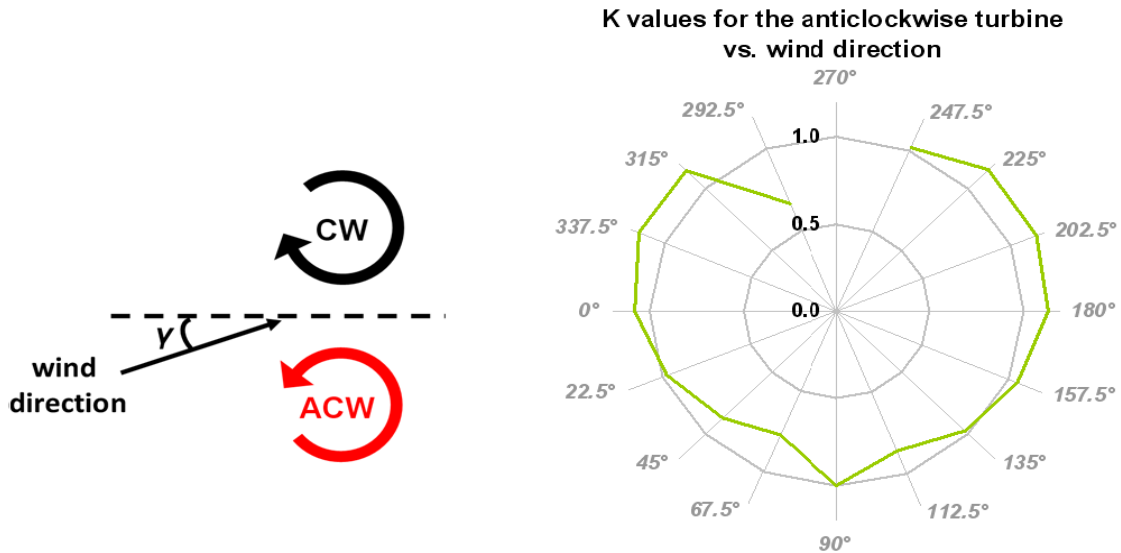
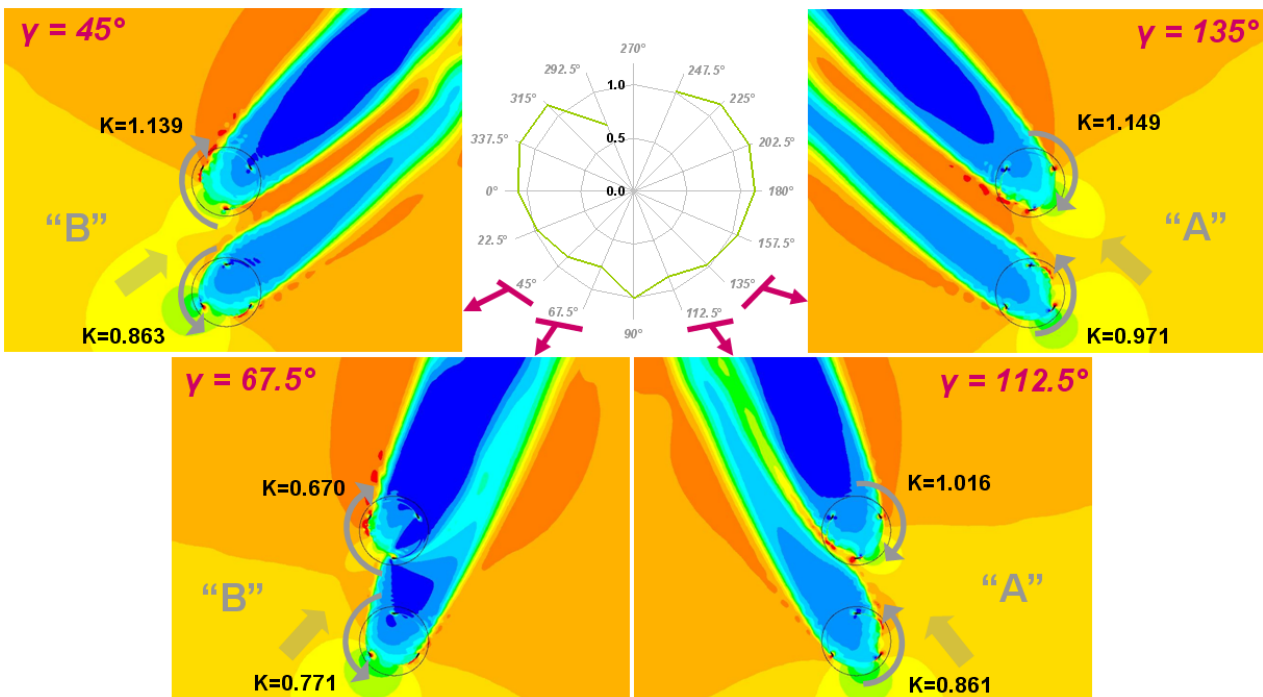


FIGURE 15: (left) turbine layout; (right) normalised power coefficient (K) of the ACW turbine versus wind direction  $\gamma$ .

404  
405  
406  
407  
408  
409  
410

The graph reveals that the turbine performance in the  $\gamma$  range  $[112.5^\circ-180^\circ-247.5^\circ]$  is better than in the  $\gamma$  range  $[292.5^\circ-0^\circ-67.5^\circ]$ . This is related to the difference in the bending of two turbine wakes in these two  $\gamma$  ranges, i.e. convergence or divergence of the two wakes, as depicted in figure 16.



411  
412  
413  
414

FIGURE 16: normalised power coefficient (K) values and velocity maps in the range  $[1 \div 10.5 \text{ m/s}]$  calculated at  $\gamma=45^\circ, 67.5^\circ, 112.5^\circ, 135^\circ$ .

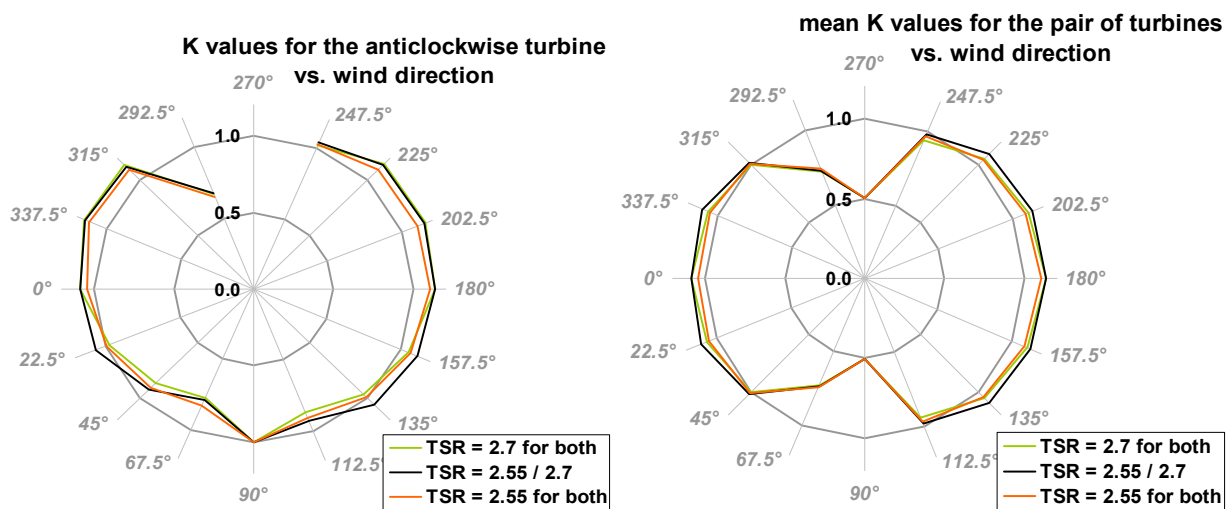
415  
416  
417  
418  
419

From this figure it can be observed that at  $\gamma=45^\circ$  and  $\gamma=67.5^\circ$  the turbines work as in the staggered-B configuration, whereas at  $\gamma=112.5^\circ$  and  $\gamma=135^\circ$  the turbines work as in the staggered-A configuration. We remark two key findings: (1) the performance of the turbines in A configurations is better than the performance of the turbines in the corresponding B configurations; and (2) with the exception of  $\gamma=67.5^\circ$ , the performance of the downstream turbine is better than the performance of the upstream one. Both these results

420 can be explained by the reasons already discussed earlier for the effect of staggering. The poor performance  
 421 of the upstream turbine at  $\gamma=67.5^\circ$  (when the convergence of the wakes occurs) is due to the backpressure  
 422 generated by the downstream turbine that, by preventing a complete development of the wake, causes a  
 423 reduction of the flow rate through the upstream turbine.

424 As the upstream turbine is affected by a lower local wind speed, it could be useful to reduce its TSR  
 425 (for instance, down to 2.55, which is the optimal value found for the isolated turbine) with keeping the  
 426 original TSR of 2.7 only for the downstream turbine (except for the cases with  $\gamma=0^\circ$  and  $180^\circ$ , where the two  
 427 turbines are side-by-side). The graphs in figure 17 show the effects of the TSR choice on the performance of  
 428 the ACW turbine and also on the average performance of the two turbines. For completeness the predictions  
 429 obtained by setting TSR=2.55 for both turbines (upstream and downstream) are also presented. The distance  
 430 between the axes is set to 2D. These results suggest that, for a given wind direction, the best performance is  
 431 obtained by setting an appropriate TSR for each of the two turbines separately.

432



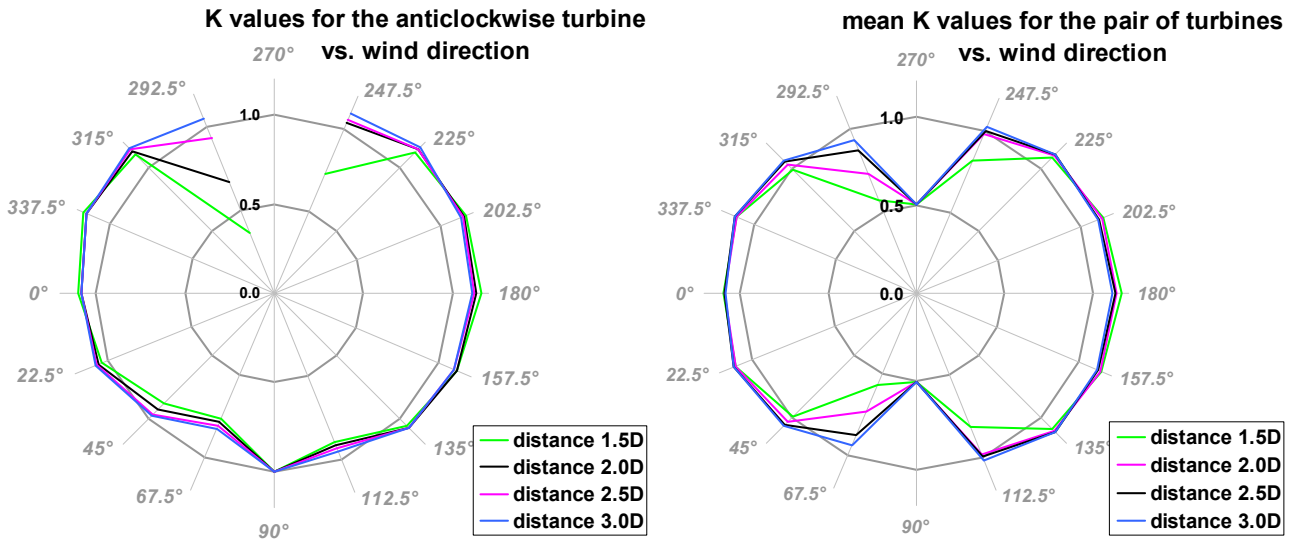
433

434 FIGURE 17: Graphs of the normalised power coefficient (K) versus wind direction in case of different rotational speed strategies, for  
 435 the ACW turbine (left) and averaged of the two turbines (right). Note: the low values of the averaged K at  $\gamma=90^\circ/270^\circ$  are due to the  
 436 assumption that only the upstream turbine is working.

437

438 Finally, the graphs in figure 18 illustrate the effects of the distance between the turbine axes on the  
 439 performance of the ACW turbine and also on the average performance of the two turbines. Four distances  
 440 are considered: 1.5D, 2D, 2.5D and 3D. TSR is set at 2.55 or 2.7 depending on the relative position of each  
 441 turbine for each wind direction. At short distances (1.5D and 2D) the performance is poor for the wind  
 442 directions that entail the downstream turbine to be located in the wake of the upstream turbine. This occurs at  
 443  $\gamma=247.5^\circ/292.5^\circ$  for the ACW turbine and, by symmetry, at  $\gamma=67.5^\circ/112.5^\circ/247.5^\circ/292.5^\circ$  for the overall  
 444 configuration. Yet for these wind directions the average power loss with respect to the isolated turbine is  
 445 quite small at longer distances, especially at a distance of 3D.

446



447  
 448 FIGURE 18: Graphs of the normalised power coefficient (K) versus wind direction at different distances between axes, for the ACW  
 449 turbine (left) and averaged of the two turbines (right). Note: the low values of the averaged K at  $\gamma=90^\circ/270^\circ$  are due to the  
 450 assumption that only the upstream turbine is working.  
 451

452  
 453 Interestingly, for the side-by-side situation ( $\gamma=0^\circ$  and  $180^\circ$ ) the effect of the turbine distance is much less  
 454 significant; hence a distance of 3D appears to be the best overall choice for varying wind directions. It is also  
 455 important to observe that, although a staggered pair cannot surpass the performance of a side-by-side pair,  
 456 for wind directions entailing the A-pair situation a distance of 3D yields nearly the same average  
 457 performance as that for the side-by-side pair for a wide range of  $\gamma$  (more than  $90^\circ$ ).  
 458

459 **Discussion**

460  
 461 The 2D CFD analysis performed in this study has explained several important flow mechanisms  
 462 regarding the performance of a counter-rotating pair of VAWTs. In this section we discuss some  
 463 implications of the current CFD results for the prediction of the performance of two typical types of VAWT  
 464 arrays and also the limitations of 2D CFD analysis for each scenario. The two scenarios to be discussed are:  
 465 (1) a single lateral row of VAWTs with each turbine counter-rotating with respect to neighbouring turbines;  
 466 and (2) multiple rows (or a farm) of counter-rotating VAWTs.

467 For the first scenario, we can expect that the performance of such a single lateral row of VAWTs will  
 468 be explained largely by the flow mechanisms investigated in this study for a pair of counter-rotating turbines.  
 469 This is because, as long as each turbine in the row is counter-rotating with respect to neighbouring turbines,  
 470 the local flow field created between any two neighbouring turbines will be similar to either A- or B-  
 471 configuration investigated in this study. One important implication here is that the mechanisms of enhanced  
 472 power generation by such a single row of VAWTs are a little more complex than the so-called “local  
 473 blockage effect” explained by the actuator disk theory [13]. As described earlier, the power generated in the  
 474 upwind path of a VAWT is affected significantly by the local velocity in the lateral (y) direction, which  
 475 cannot be explained by the 1D actuator disk theory. It should be noted that the 2D CFD analysis performed

476 in this study also has some limitations compared to a full 3D analysis. Presumably the most important  
477 limitation is that the recovery rate of turbine wakes predicted by 2D CFD, especially in the far-wake region,  
478 is usually lower than a full 3D case due to the lack of vertical mixing. However, for the case of a single row  
479 of VAWTs, we can expect that the details of far-wake mixing will not affect the local flow characteristics  
480 around each turbine (except when the wind direction is close to  $\gamma=90^\circ/270^\circ$ , where turbines will be in the  
481 wake of other turbines). This means that the local flow mechanisms explained by the current 2D CFD are of  
482 direct relevance to the performance of a single row of VAWTs, as long as the aspect ratio of each turbine  
483 (the ratio of the blade length to the rotor diameter) is large enough to neglect the blade tip effects.

484 For the second scenario, where turbines are arrayed not only in the lateral but also in the stream-wise  
485 directions to form a VAWT farm, the local flow mechanisms investigated in the current 2D CFD are still  
486 expected to be of some importance. The performance of turbines in the most upstream part of the farm may  
487 still be explained in a similar manner to the single row case, although that in the downstream part of the farm  
488 would be affected by the details of far-wake mixing behind each turbine and also by the reduction of overall  
489 flow rate through the entire farm due to the transfer of momentum in the vertical direction, which cannot be  
490 predicted by a 2D analysis. It should be noted that the importance of the local flow mechanisms to the  
491 overall performance of the farm is likely to depend on the size of the farm. For a relatively small farm with  
492 only a few rows of VAWTs, we can presume that the local flow mechanisms investigated in this study would  
493 still be of dominant importance, since the majority of the turbines in the farm would not be significantly  
494 affected by the wake of other turbines. For a much larger farm, however, the local flow mechanisms would  
495 be of less importance, since the majority of the turbines in the farm would be in the wake of other turbines as  
496 well as be influenced by the reduction of overall flow rate through the farm. In such a large farm, the main  
497 benefit of employing counter-rotating VAWTs could be that the wake loss is reduced and thus a high-speed  
498 flow is maintained throughout the farm, as suggested by Dabiri [2], in analogy with the mechanism of “fish  
499 schooling”. The recent study by Araya et al. [4] aims to describe approximately the mechanism of this farm-  
500 power enhancement using a low-order flow model; however the model is 2D and is therefore not capable of  
501 predicting the reduction of overall flow rate through the farm correctly. Further investigations are required to  
502 understand the performance of such a large VAWT farm.

503

## 504 **Conclusions**

505

506 In this study we have performed an extensive and detailed 2D CFD analysis of flow around a pair of  
507 counter-rotating VAWTs to identify the local flow mechanisms contributing to their enhanced power  
508 generation performance compared to an isolated VAWT. The analysis was performed for two possible  
509 configurations of the counter-rotating turbine pair (namely A and B configurations) with various gaps  
510 between the two turbines, tip-speed-ratios and wind directions.

511 For the case of two turbines arrayed side-by-side with respect to the incoming wind (i.e. wind direction  
512  $\gamma=0^\circ/180^\circ$ ), we have found two key mechanisms contributing to the power increase: (1) change of lateral (y)  
513 velocity in the upwind path due to the presence of the neighbouring turbine, making the direction of local



514 flow approaching the blade more favourable to generate lift and torque in the upwind path; and (2)  
515 contraction of the wake in the downwind path, again due to the presence of the neighbouring turbine, making  
516 a larger momentum flux available for power generation in the downwind path. The balance between the two  
517 mechanisms (in terms of their contributions to the overall power increase) has been found to depend on the  
518 tip-speed-ratio as well as on the configuration type (A or B).

519 For the case of two turbines arrayed in a staggered pattern with respect to the incoming wind, we have  
520 observed that a larger power tends to be generated by the downstream turbine than by the upstream turbine  
521 (unless the downstream turbine is in the wake of the upstream turbine). This is essentially due to the  
522 upstream turbine blockage, making a high-speed flow available to the downstream turbine. However, the  
523 total power of a staggered pair of turbines cannot surpass that of a side-by-side pair of turbines. The total  
524 power of a pair of turbines decreases significantly when the wind direction is close to  $\gamma=90^\circ/270^\circ$ , and the  
525 value of  $\gamma$  at which this significant power decrease occurs depends on the configuration type (A or B). The  
526 power tends to remain high for the A-configuration, i.e. when the velocity induced between the two turbines  
527 is concordant with the wind direction, since the two turbine wakes in this configuration tend to diverge from  
528 each other and hence the downstream turbine is less likely to be in the wake of the upstream turbine.

529 Finally, we have also discussed some implications of the current 2D CFD results for the prediction of  
530 the performance of two typical types of VAWT arrays, namely a single row of counter-rotating VAWTs and  
531 multiple rows (or a farm) of counter-rotating VAWTs. For the former case, we can expect that the  
532 performance of such a single row of VAWTs will be explained largely by the local flow mechanisms  
533 investigated in this study, since the local flow field created between any two neighbouring turbines in such a  
534 single row will be similar to either A- or B-configuration studied here. For the latter case, the flow  
535 mechanisms investigated in this study are still expected to be of some importance, especially when the farm  
536 size is relatively small. As the farm size increases, however, the overall performance of the farm would  
537 depend more and more on the details of far-wake mixing of each turbine and also on the reduction of overall  
538 flow rate through the farm due to the transfer of momentum in the vertical direction, which cannot be  
539 assessed by 2D CFD. Further investigations are therefore required to understand the performance of such a  
540 large VAWT farm.

541

## 542 **Appendix**

543

544 All simulations described in the paper were performed with a reasonably fine grid (grid (1));  $y^+$  is less  
545 than 3 except for the trailing edge, where few elements with  $y^+ \sim 5$  appear due to the difficulty to generate  
546 regular and small quad elements on a sharp trailing edge. To investigate the grid sensitivity, some  
547 simulations are repeated with a new grid (grid (2)) employing a rounded trailing edge, with a radius of 0.5%  
548 of the chord length, allowing the regular growing of quad elements all around the trailing edge, and a smaller  
549 wall distance from the first layer of cells, resulting in  $y^+ < 0.5$  all around the blade. An additional finer grid  
550 (grid (3)), characterised by a greater number of elements on the blade profile and on the interface between  
551 steady and rotating domains, is also tested. The main grid features are summarised in table 2.

552

Case name	$y^+$	Nodes on blade profile	Nodes on rotating interface	Cells in each rotating domain	Total domain cells for the isolated turbine case	Total domain cells for the turbine pair case
Grid (1)	< 3	440	720	117000	246000	383000
Grid (2)	< 0.5	440	720	131000	260000	411000
Grid (3)	< 0.5	700	1200	246000	385000	666000

TABLE 2: Main features of the grids adopted for the grid sensitivity study.

553  
554

555 Simulations are performed for the isolated turbine and for the A-pair (with a distance between axes of  $1.5D$ )  
556 with a TSR of 2.7 (the optimal TSR in case of the pair configuration). Results show that, for both isolated  
557 turbine and A-pair cases, a slightly lesser flow separation during the upwind path is observed with grid (2)  
558 than with grid (1), and with grid (3) than with grid (2). Correspondingly, a slightly greater pressure  
559 difference between the suction and the pressure sides of the blade is observed with a slightly lesser flow  
560 separation during the upwind path. Eventually, the instantaneous one-blade  $C_p$  variations depicted in figures  
561 19 and 20 show that the grid refinements lead to a slightly greater maximum power.  
562

563  
564  
565

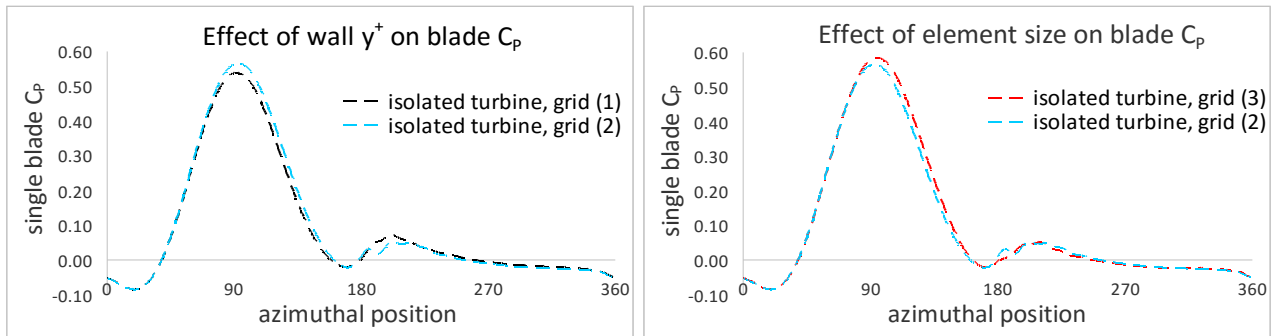


FIGURE 19: Effect of grid refinement on the instantaneous one blade  $C_p$  in the case of isolated turbine.

566  
567  
568

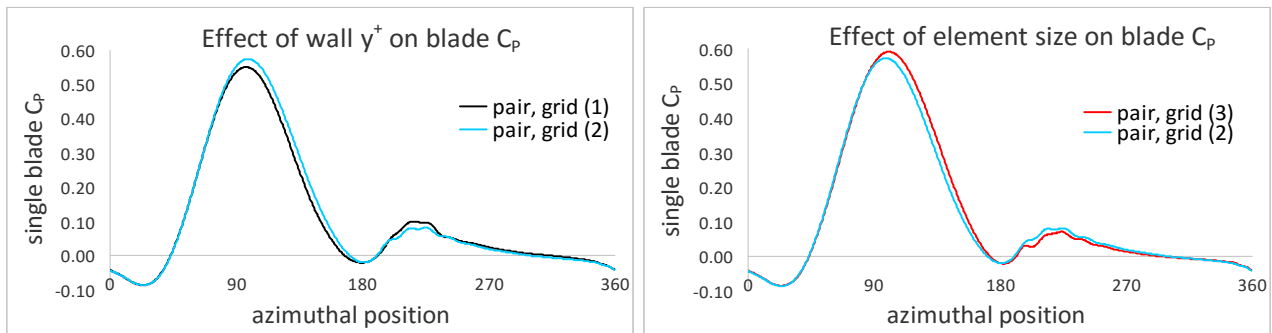


FIGURE 20: Effect of grid refinement on the instantaneous one blade  $C_p$  in the case of A-pair.

Case name	$C_p$ isolated turbine	$C_p$ pair	power ratio: $C_{p,pair}/C_{p,isolated}$	$((\text{power ratio}) - (\text{power ratio})_{\text{grid}(1)}) / (\text{power ratio})_{\text{grid}(1)}$
Grid (1)	0.274	0.321	1.171	-
Grid (2)	0.287	0.336	1.172	0 %
Grid (3)	0.300	0.348	1.160	-0.94 %

TABLE 3: Main results of the grid sensitivity study.

569  
570

571 Table 3 summarises the turbine performance obtained in terms of the absolute  $C_p$  and of the “power ratio”,  
572 i.e. normalised power gain for the A-pair case with respect to the isolated turbine case. The results obtained  
573 with the grid (3) are considered to be more accurate in terms of the absolute turbine performance, but require  
574 much more computational resources than the grids (1) and (2). Yet, the most important conclusion from this  
575 grid sensitivity study is that, despite the non-negligible effects of  $y^+$  and element size on the absolute turbine  
576 performance, there are no significant effects on the power gain for the turbine pair with respect to the  
577 isolated turbine. Since the main focus of the present paper is on the behaviour of a pair of turbines compared  
578 to the behaviour of the isolated turbine, even grid (1) can be considered sufficiently accurate.

## 579 580 **References**

- 581 [1] Whittlesey R. W., Liska S. and Dabiri J. O., “Fish schooling as a basis for vertical axis wind turbine farm design”, *Bioinspiration*  
582 & *biomimetics*, 2010, vol.5
- 583 [2] Dabiri J. O., “Potential order-of-magnitude enhancement of wind farm power density via counter-rotating vertical-axis wind  
584 turbine arrays”, *Journal of renewable and sustainable energy*, 2011, vol. 3
- 585 [3] Kinzel M., Mulligan Q. and Dabiri J. O., “Energy exchange in an array of vertical-axis wind turbines”, *Journal of Turbulence*,  
586 2012, vol. 13, No. 38, pp. 1–13
- 587 [4] Feng G. et al. “Optimizing the Land Use for Wind Farms Using Vertical Axis Wind Turbines”, PO.ID 192, Europe's premier  
588 wind energy conference and exhibition, European Wind Energy Association (EWEA), 2014, Barcelona, Spain.
- 589 [5] Araya D. B., Craig, A. E., Kinzel, M., Dabiri, J. O., “Low-order modeling of wind farm aerodynamics using leaky Rankine  
590 bodies”, *Journal of renewable and sustainable energy*, 2014, vol. 6, 063118.
- 591 [6] F. Balduzzi, A. Bianchini, R. Maleci, G. Ferrara, L. Ferrari, Critical issues in the CFD simulation of Darrieus wind turbines,  
592 *Renewable Energy* 85 (2016) 419-435.
- 593 [7] Windward Engineering. Power Performance Test Report for Windspire, 2013, [http://windwardengineering.com/our-](http://windwardengineering.com/our-work/projects/windspire/windspire-rtc-testing/)  
594 [work/projects/windspire/windspire-rtc-testing/](http://windwardengineering.com/our-work/projects/windspire/windspire-rtc-testing/)
- 595 [8] Ansys Fluent 12.0. User's Guide, Ansys Inc. (2009).
- 596 [9] F. R. Menter, “Zonal two equation k-omega model for aerodynamic flows”, in: 24th Fluid Dynamics Conference, July 6-9,  
597 Orlando, Florida, 1993.
- 598 [10] Nobile R, Vahdati M, Barlow JF, Mewburn-Crook A. “Unsteady flow simulation of a vertical axis augmented wind turbine: A  
599 two-dimensional study”, *J. Wind Eng. Ind. Aerodyn.*125 (2014) 168–179.
- 600 [11] M. C. Claessens, “The Design and Testing of Airfoils for Application in Small Vertical Axis Wind Turbines”, Master of Science  
601 Thesis, Faculty of Aerospace Engineering, Delft University of Technology, November 9th, 2006.
- 602 [12] S. Giorgetti, G. Pellegrini, S. Zanforlin, “CFD investigation on the aerodynamic interferences between medium-solidity Darrieus  
603 vertical axis wind turbines”, *Energy Procedia* 81 (2015) 227-239.
- 604 [13] Nishino T., Draper S., “Local blockage effect for wind turbines”, *Journal of Physics: Conference Series*, 2015, vol. 625, 012010.